optica

Room-temperature InP/InGaAs nano-ridge lasers grown on Si and emitting at telecom bands

Yu Han,[1] Wai Kit Ng,[2] Chao Ma,[2] Qiang Li,[1] Si Zhu,[1] Christopher C. S. Chan,[2] Kar Wei Ng,[3] Stephen Lennon,[4] Robert A. Taylor,[4] Kam Sing Wong,[2] and Kei May Lau[1],*

[1]Department of Electronic and Computer Engineering, Hong Kong University of Science and Technology, Clear Water Bay, Kowloon, Hong Kong, China
[2]Department of Physics, Hong Kong University of Science and Technology, Clear Water Bay, Kowloon, Hong Kong, China
[3]Institute of Applied Physics and Materials Engineering, University of Macau, Avenida da Universidade, Macau, China
[4]Clarendon Laboratory, Department of Physics, University of Oxford, Oxford OX1 3PU, UK
*Corresponding author: eekmlau@ust.hk

Semiconductor nano-lasers grown on silicon and emitting at the telecom bands are advantageous ultra-compact coherent light sources for potential Si-based photonic integrated circuit applications. However, realizing room-temperature lasing inside nano-cavities at telecom bands is challenging and has only been demonstrated up to the E band. Here, we report on InP/InGaAs nano-ridge lasers with emission wavelengths ranging from the O, E, and S bands to the C band operating at room temperature with ultra-low lasing thresholds. Using a cycled growth procedure, ridge InGaAs quantum wells inside InP nano-ridges grown on patterned (001) Si substrates are designed as active gain materials. Room-temperature lasing at the telecom bands is achieved by transferring the InP/InGaAs nano-ridges onto a SiO_2/Si substrate for optical excitation. We also show that the operation wavelength of InP/InGaAs nano-lasers can be adjusted by altering the excitation power density and the length of the nano-ridges formed in a single growth run. These results indicate the excellent optical properties of the InP/InGaAs nano-ridges grown on (001) Si substrates and pave the way towards telecom InP/InGaAs nano-laser arrays on CMOS standard Si or silicon-on-insulator substrates. © 2018 Optical Society of America under the terms of the OSA Open Access Publishing Agreement

OCIS codes: (140.3410) Laser resonators; (140.3948) Microcavity devices; (230.5590) Quantum-well, -wire and -dot devices.

https://doi.org/10.1364/OPTICA.5.000918

1. INTRODUCTION

Direct integration of III-V light emitters and optical amplifiers onto Si substrates as inter/intra chip optical interconnects is the key for high-functionality and low-cost photonic integrated circuits (PICs) [1,2]. III-V nano-lasers with an extremely small footprint and ultra-low energy dissipation could further benefit Si-based PICs in terms of integration density and power consumption [3–7]. To be compatible with passive Si optical components such as waveguides, couplers, and splitters, on-chip light sources must emit at silicon transparent wavelengths (larger than 1150 nm) to minimize propagation loss. Furthermore, inter-chip coupling with minimum loss by optical fibers requires light emission at the telecom bands (from 1260 to 1625 nm) [8]. Lasing operation at the O band (1260 to 1360 nm) has been demonstrated from InP/InGaAs distributed feedback nano-ridges, vertical free-standing InP/InGaAs nano-pillars, and InP/InAsP nanowires transferred onto a photonic crystal cavity [9–11]. Recently, room-temperature lasing up to the E band (1360 to 1460 nm) has been realized using InGaAs/InGaP photonic crystal nano-beam cavities [12]. Extending the lasing spectra to the S band (from 1460 to 1530 nm) and the C band (from 1530 to 1565 nm) could greatly improve the bandwidth density and

circuit functionality of Si PICs. However, achieving laser oscillation inside nano-cavities at longer wavelengths is extremely challenging due to the escalating loss mechanisms associated with increasing wavelength. The weak confinement of photonic modes at long wavelengths inside sub-micrometer laser cavities induces a large propagation loss, and the optical feedback from the end facets of the Fabry–Perot cavities decreases as the wavelength increases [13]. Additionally, non-radiative free-carrier absorption and Auger recombination at high carrier injection levels exacerbate this situation [2]. Even though lasing operation at the C band has been observed in bulk GaSb nanowires, the nano-lasers were tested at cryogenic temperatures and featured a relatively large cross-sectional dimension (700 to 1500 nm) [14].

To fully exploit the capabilities offered by CMOS foundries for Si photonics, light-emitting III-V nano-structures should, ideally, be grown on industrial-standard (001) Si substrates without any intentional offcut. The aspect ratio trapping (ART) technique has produced various high-quality III-V nano-ridge arrays, such as GaAs, InP, InGaAs, GaSb, and InAs, inside Si trenches confined by SiO_2 spacers on exact (001) Si substrates [15–22]. To attain laser operation using III-V nano-ridges grown by ART, the active gain material should be carefully designed to minimize the

influence of crystalline defects, and the optical modes should be well confined inside the III-V gain material. Three methods have been developed to minimize light leakage into the underlying Si substrates; they include selective etching away of the underlying silicon to obtain suspended III-V nano-ridges in the air [23], growth of large III-V ridge structures out of narrow trenches [24], and direct growth of the III-V nano-ridges on silicon-on-insulator (SOI) wafers [25]. While strong on-chip mode confinement inside the III-V nano-ridges has been demonstrated, the active gain material has yet been carefully designed to sustain room-temperature lasing at the telecom bands [26–29].

In this work, we demonstrate room-temperature sub-wavelength InP/InGaAs nano-ridge lasers emitting at telecom bands up to 1533 nm. Ridge InGaAs quantum wells (QWs) separated by InP spacers are designed as the active gain material, and light emission is carefully tuned to cover the whole range of telecom bands. Using 450 nm wide InP/InGaAs nano-ridges grown on (001) Si substrates, we achieve room-temperature lasing at the O, E, S, and C bands after transferring the nano-ridges onto a SiO$_2$/Si substrate. We also show that the lasing modes exhibit strong dependence on the excitation levels and the length of the nano-ridges. The lasing modes at longer wavelengths usually dominate under low excitation levels, while modes at shorter wavelengths would prevail under high excitation levels. We demonstrated for the first time to our knowledge that the lasing wavelength can be adjusted over a wide band, from the 1300 nm band up to the 1500 nm band, by changing the excitation levels and the length of the nano-ridges. Compared with controlling the lasing wavelength via tuning the indium fraction of the InGaAs crystallized in several growth runs [4,12], tailoring the lasing wavelengths in multiple bands by altering the length of the nano-ridges with the same epi-structure formed in a single growth run betokens practical applications for Si photonics.

2. GROWTH AND FABRICATION

The in-plane InP/InGaAs nano-ridge array was selectively grown on patterned (001) Si substrates using a metal organic vapor deposition system (AIXTRON 200/4). The detailed growth procedure can be found in Refs. [27] and [28]. We did not intentionally introduce any dopant during the hetero-epitaxy process, and the background doping should be lightly n-type. Figure 1(a) shows the 70° tilted view scanning electron microscope (SEM)

image of an as-grown sample, manifesting a highly ordered InP/InGaAs nano-ridge array inside nano-scale trenches. The cross-sectional transmission electron microscopy (TEM) photo of one typical InP/InGaAs nano-ridge imaged using a JEOL2001F microscope is displayed in Fig. 1(b). The InP/InGaAs nano-ridge has a width of 450 nm and a height of 1.0 μm (from the top tip to the bottom tip). Anti-phase boundaries are eliminated by initiating the material deposition at exposed {111} Si surfaces [30]. The 8% lattice mismatch between InP and Si is accommodated through an ultra-thin (∼10 nm) GaAs stress-reducing buffer and the formation of a high density of defects at the III-V/Si interface [see the dark area in Fig. 1(b)]. The InP buffer layer, where five InGaAs ridge QWs are embedded, has been optimized with much reduced interfacial defects. The ridge structure with two convex {111} facets are developed to minimize the total surface energy during the hetero-epitaxy process and is commonly observed in other III-V nano-structures grown by ART [31,32]. Figure 1(c) presents a zoomed-in TEM image of the InGaAs ridge QWs at one side of the InP nano-ridge. The InGaAs ridge QWs exhibit an average thickness of 8 nm. An indium composition of 53% is extracted from the X-ray diffraction measurement of a sample with a thick InGaAs calibration layer. The InP spacers, showing an average thickness of 22 nm, can effectively suppress electron tunneling from adjacent QWs. The high-resolution TEM image of one InGaAs QW in Fig. 1(d) reveals atomic sharp InP/InGaAs interfaces and thus, minimized non-radiative recombination via interface states.

Direct epitaxy of a InGaAs layer on a multi-faceted InP buffer often leads to carrier localization at the crossover region of the {111} facets due to growth preference at the InP tip and composition inhomogeneity, which drains the electrons of the ridge QWs and jeopardizes the material gain [33]. We developed a unique growth procedure for each InGaAs ridge QW to obliterate the carrier localization and achieve a uniform carrier distribution inside the active region. The deposition of each InGaAs ridge QW consists of eight identical cycles at 600°C. Each cycle includes a 6 s InGaAs growth with triethylgallium (TEGa), tertiarybutylarsine (TBA), and trimethylindium (TMIn) introduced into the reactor and a 30 s growth interruption in a TBA ambient. The growth interruption allows the adatoms to redistribute along the different facets of the InP ridge buffer. The efficacy of the cycled
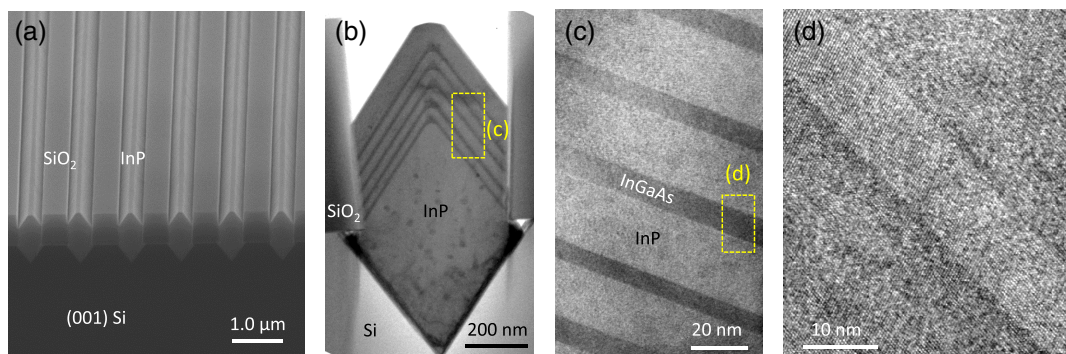

Fig. 1.   (a) 70° tilted SEM image of the highly ordered, in-plane InP/InGaAs nano-ridge structures on (001) Si substrates. (b) Cross-sectional TEM image of the InP/InGaAs nano-ridge perpendicular to the wire direction, showing five {111} ridge InGaAs QWs embedded inside a InP nano-ridge; the dark area at the InP/Si interface contains a high density of stacking faults generated for strain relaxation. (c) Zoomed-in TEM image of the five InGaAs QWs separated by InP spacers at one side of the InP nano-ridge. (d) High-resolution TEM image of one InGaAs ridge QW with atomic sharp InP/InGaAs interfaces.
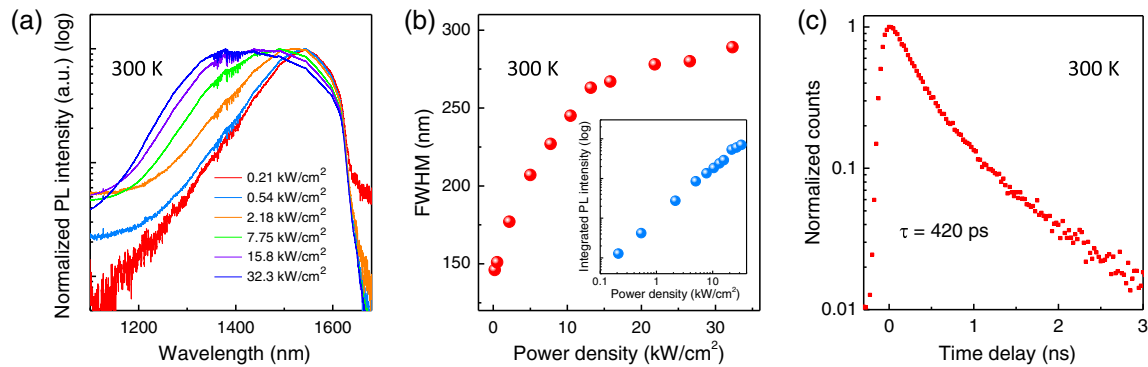
Fig. 2. (a) Room-temperature PL spectra of the five InGaAs QWs under different excitation levels at the telecom bands, revealing apparent band-filling effects and broadening of the PL spectra. (b) Widening of the FWHM of the PL spectra as pumping power increases; the inset shows the linear evolution of integrated PL intensity as a function of pumping power. (c) Time-resolved PL data of the as-grown InP/InGaAs nano-ridges, revealing a carrier lifetime of 420 ps.

growth process is attested by notable changes of the photoluminescence (PL) spectra from broad double-peaked spectra without growth interruption to narrow single-peaked spectra with a 30 s cycled growth interruption. Figure 2(a) displays the PL spectrum of the InGaAs ridge QWs under different excitation levels measured at room temperature. At a low pumping power density of 0.21 kW/cm^2, the peak of the PL spectra sits around 1545 nm, corresponding to light emission from the band edges. As the pumping density increases, the peak gradually shifts to shorter wavelengths, and the full width half-maximum (FWHM) expands from 146 nm at 0.21 kW/cm^2 to 289 nm at 32.3 kW/cm^2, indicating apparent band-filling effects [see Fig. 2(b)]. The relatively large FWHM of the PL spectra is partially a result of the thickness variation of the ridge QWs [see Fig. 1(c)]. The integrated PL intensity exhibits a linear relationship with the pumping level as shown by the inset in Fig. 2(b). We also performed time-resolved PL measurements to study the minority carrier lifetime of the InGaAs ridge QWs. Figure 2(c) depicts the PL decay of the InGaAs ridge QWs, and a carrier lifetime $\tau = 420$ ps is extracted from the mono-exponential fits. The carrier lifetime of a semiconductor typically depends on three different recombination mechanisms: non-radiative recombination via defects, band-to-band radiative recombination, and non-radiative Auger recombination. At room temperature and under a low excitation level, the measured τ should refer to the defect-related non-radiative carrier lifetime and thus is directly associated with the crystalline quality of the material. The carrier lifetime of the InGaAs ridge QWs is on par with that of lightly carbon-doped (10^{16} cm^{-3}) strained InGaAs grown on InP substrates [34], InGaAs/InGaP nano-pillars grown on Si [35], and AlGaAs-passivated GaAs nanowires [5].

To investigate the suitability of the InP/InGaAs nano-ridges as coherent light sources at the telecom bands, we detached the nano-ridges from the as-grown substrates and transferred them onto a SiO$_2$/Si substrate with 1.0 μm thick oxide for optical characterization. Figure 3(a) schematically summarizes the transfer process, which involves the removal of the oxide spacers and the undercut of the underlying Si followed by sonication in an ultrasonic bath. During the sonication, the nano-ridges peeled off from the initial Si substrate and fragmented into different lengths. The fractured surfaces of the nano-ridge serve as the end-facets of the nano-cavity. Figure 3(b) shows the top-view
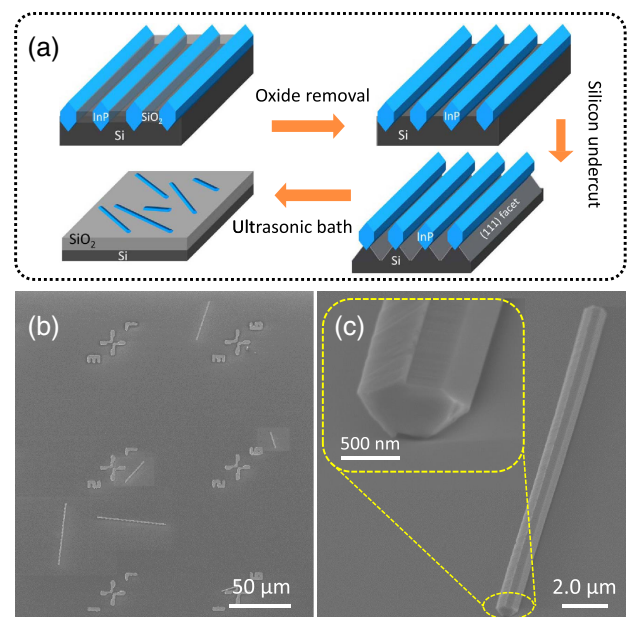

Fig. 3. (a) Schematics showing the transfer of the as-grown InP/InGaAs nano-ridges onto a SiO$_2$/Si substrate. (b) Top-view SEM image of the transferred InP/InGaAs nano-ridges with different orientations and lengths. The length of the nano-ridges ranges from 10 to 80 μm. (c) 70° tilted SEM image of one transferred InP/InGaAs nano-ridge; the inset shows a smooth and vertical end facet.

SEM image of the transferred InP/InGaAs nano-ridges with random orientations. The length of the nano-cavities fragmented during sonication varies from 10 to 80 μm, and the markers on the oxide allow us to precisely locate each measured nano-ridge. A 70° tilted view SEM image in Fig. 3(c) illustrates the Fabry–Perot (FP) cavity with two end facets, and the inset displays one end facet with a smooth fracture surface and a (110) orientation.

3. RESULTS AND DISCUSSION

The transferred InP/InGaAs nano-ridges were optically excited by a 750 nm Ti/Sapphire laser, delivering 100 fs pulses at a 76 MHz
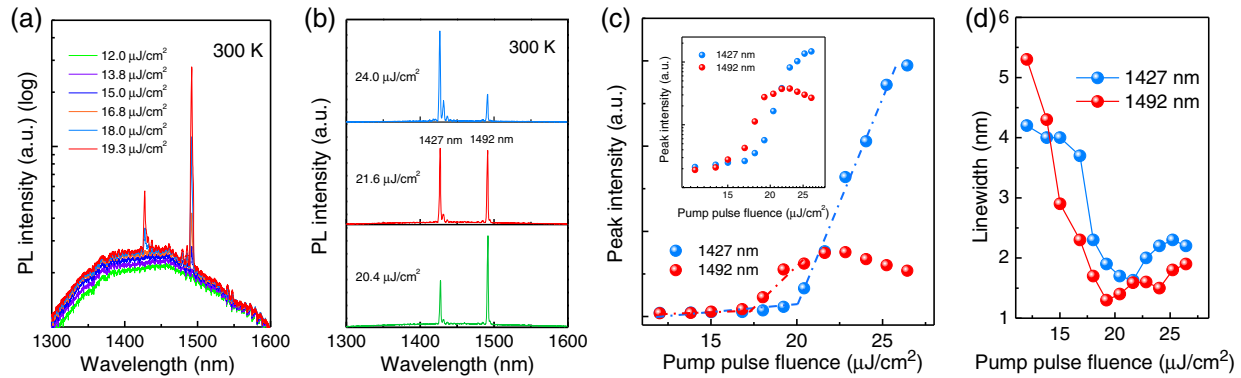
Fig. 4. (a) Room-temperature PL spectra of one InP/InGaAs nano-ridge with a length of 38 μm under different excitation levels plotted in a log scale, showing broad spontaneous emission spectra with equally spaced FP modes below the threshold and the clamp of spontaneous emission and sudden increase of the mode at 1492 nm when pumping level increases above the threshold. (b) PL spectra of the InP/InGaAs nano-laser above the threshold. The mode at 1427 nm gradually increases and finally dominates over the mode at 1492 nm. (c) L–L curves of the two modes at 1492 nm and 1427 nm plotted on a linear scale. The threshold of the modes at 1492 nm and 1427 nm are extracted as 16.0 μJ/cm² and 19.0 μJ/cm², respectively. The inset shows the L–L curves on a logarithmic scale, revealing a clear S shape for both the two modes. (d) Evolution of the linewidth of the modes as a function of the pumping pulse fluence. The linewidth narrowing around the threshold further confirms the lasing behavior.

repetition rate. With a cylindrical lens placed in the incident optical path, the excitation laser was focused into a line-shaped spot with a size of 68 μm × 2 μm to cover the entire laser cavity. By simply rotating the cylindrical lens, we could measure nano-ridges with different orientations. Figure 4 exemplifies the room-temperature lasing behavior of one InP/InGaAs nano-ridge with a length of 38 μm. The emission spectra measured near the threshold are plotted in a log scale in Fig. 4(a). Under low excitation levels, the emission shows broad spontaneous spectra with discernible longitudinal FP modes. Using the relation given by $\Delta\lambda = \lambda^2/2Ln_g$, where L is the length of the laser cavity and $\Delta\lambda$ refers to the spacing of adjacent longitudinal modes, a group reflective index of $n_g = 4.8$ is extracted. As the excitation level increases to 18.0 μJ/cm², the mode at 1492 nm in the S band reaches the threshold, intensifies, and stands out from the clamped spontaneous emission, indicating the onset of lasing. As shown by the emission spectra above the threshold in Fig. 4(b), another lasing peak at 1427 nm in the E band appears under a pumping pulse fluence of 20.4 μJ/cm², equals the mode at 1492 nm under a pumping level of 21.6 μJ/cm², and finally dominates as the pumping level continues to increase. Figure 4(c) plots the peak emission intensity of the modes at 1492 nm and 1427 nm as a function of the pumping pulse fluence. We detect a clear knee behavior for both modes from the light–light (L–L) curves, and thresholds of 16.0 μJ/cm² and 19.0 μJ/cm² are deduced for the modes at 1492 nm and 1427 nm, respectively. Because of the longer length of the FP cavity and resultant higher light amplification per round-trip, the lasing thresholds of the InP/InGaAs nano-ridge laser are much lower than those of other III-V nano-lasers in the near-infrared range [4,5,10,12]. The lasing behavior is further attested by the clear S-shape of the L–L curves plotted in a log scale [see the inset of Fig. 4(c)] and the abrupt narrowing of the linewidth around the lasing threshold [see Fig. 4(d)]. Note that the slope efficiency of the peak at 1427 nm is higher than that of the peak at 1492 nm. This behavior can be explained by the higher material gain at high excitation levels and lower round-trip loss of shorter wavelengths. The intensity of the first-lasing mode starts to decrease around 22.8 μJ/cm², possibly due to the competition for material gain.

Additionally, the modal gain of shorter wavelengths is larger than that of longer wavelengths due to the better optical confinement, and thus oscillation at shorter wavelengths would dominate under high pumping intensities. The phenomenon of lasing from multi-longitudinal modes, featuring initial lasing at longer wavelengths and then moving to shorter wavelengths, is observed in most of the measured InP/InGaAs nano-ridge lasers. We simulated the distribution of electrical field intensity inside the InP/InGaAs waveguide, and the lasing transverse mode is most likely to be TE$_{01}$ due to the largest overlap with the active gain material.

In addition to the dependence on the excitation level, the lasing wavelength also manifests a strong correlation with the length of the nano-ridges. Figure 5(a) presents the room-temperature lasing spectra just above the threshold of eight InP/InGaAs nano-ridges with increasing lengths from 13 to 51 μm. The lasing wavelength spreads from 1356 to 1533 nm as the length of the nano-ridge increases. We also observe a quasi-linear dependency between the operation wavelength and the length of the nano-ridges, as shown in Fig. 5(b). Notably, with the InGaAs ridge QWs in a single growth run as the gain material, the operation wavelength of the InP/InGaAs nano-ridge lasers could be varied continuously from the O band to the C band by modifying the length of the FP cavity. Note that the excitation level also plays a vital role in the selection of lasing wavelengths. Lasing at the blue side of the spectrum necessitates a higher excitation power to trigger the band-filling effects. The adjustable wavelength suggests potential applications of nano-ridge lasers with defined cavity lengths in wavelength-division multiplexing (WDM) systems with single-mode lasing selection schemes. We attribute the slight fluctuation of the data points from the quasi-linear trend in Fig. 5(b) to the difference in the quality of the end facets. More precise control of the operation wavelength can be achieved with better end-facet quality and uniformity, obtained by dry etching or focused ion beam milling. The widely adjustable range of the lasing wavelengths stems from the broad spontaneous emission spectra of the InGaAs/InP QWs. With a well barrier over 0.54 eV, InGaAs/InP QWs can provide material gain for wavelengths in all the telecom bands. In addition, the thickness inhomogeneity of the ridge QWs further broadens the gain
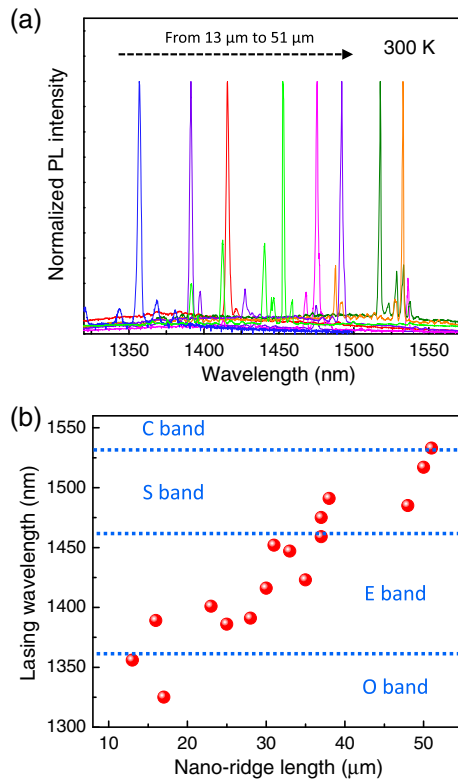
Fig. 5. (a) Room-temperature lasing spectra of InP/InGaAs nano-lasers with different lengths ranging from 13 to 51 µm. The first lasing peaks of the nano-ridge lasers cover the spectrum from 1356 to 1533 nm. (b) Evolution of the lasing wavelengths as function of the nano-ridge lengths. The laser emission covers the majority of the telecom bands, ranging from the O band to the C band.
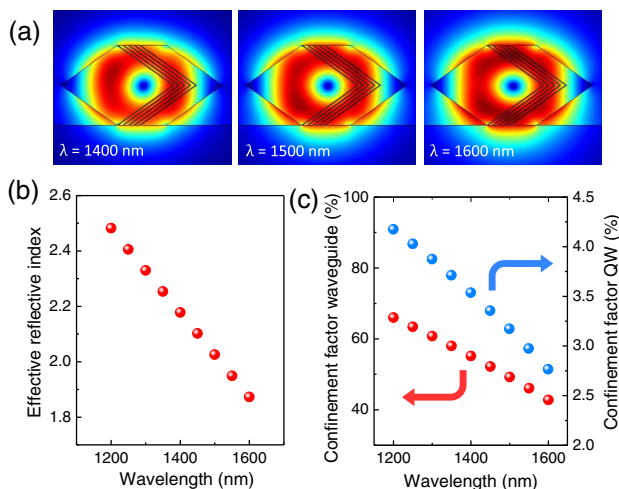
Fig. 6. (a) Simulated guided modes inside the InP/InGaAs nano-ridges at different wavelengths. (b) Calculated effective reflective index of TE01 at different mode wavelengths. (c) Confinement factors of both the InP waveguide and InGaAs QWs decrease monotonously as the mode wavelengths increases.

spectrum. The modulation of the operation wavelength with the length of the nano-ridge is closely associated with the dissimilarity of the round-trip gain and loss between different wavelengths. Figure 6(a), presenting the mode profiles at 1400, 1500, and

1600 nm, reveals an increasing light leakage into the surroundings as the mode wavelength increases. We also found that the effective reflective index and the confinement factors of the lasing transverse mode TE$_{01}$ inside the InP waveguide and the InGaAs QWs decrease monotonically with the mode wavelength, suggesting an increasing propagation loss and a reducing modal gain [see Figs. 6(b) and 6(c)]. Besides, the optical feedback from the end facets also diminishes with increasing wavelength. With a cavity length larger than 10 µm, the peaks of the FP modes overlapping with the gain spectrum would blue-shift as the excitation level increases. The optical mode that experiences the highest gain and lowest loss will lase. For InP/InGaAs nano-lasers with a short cavity length and thus limited gain material, only shorter wavelengths can reach the threshold because of the larger modal gain under high injection levels and lower round-trip loss, while for InP/InGaAs nano-lasers with a long cavity length and a substantial volume of gain material, even the long wavelengths could experience enough optical amplification to compensate for the large round-trip loss.

4. CONCLUSION

In conclusion, we demonstrated room-temperature InP/InGaAs nano-ridge lasers with adjustable wavelengths ranging from the 1300 nm band to the 1500 nm band. By initiating a cycled growth procedure, InGaAs ridge QWs with excellent optical properties are designed as an active gain material. Room-temperature lasing operation at the telecom bands from the InP/InGaAs nano-ridges initially grown on CMOS standard (001) Si substrates indicates the high crystalline quality of the InP/InGaAs nano-ridge structures and suggests the potential of integrating nano-scale light sources onto the industrial-standard Si photonics chips. Tuning the lasing wavelengths in the telecom bands by varying the pumping level and the length of the FP cavities signifies potential applications for compact WDM systems.

Practical applications in Si photonics requires on-chip electrically injected single-mode nano-lasers emitting at the telecom bands. With the current in-plane configuration, doping of the III-V nano-ridges inside Si trenches is achievable. In fact, highly doped InAs, InGaAs, GaAs, and InP nano-ridge structures have already been reported in InGaAs gate-all-around FinFets [36] and GaAs/InGaAs fin-array tunnel diodes [37]. Among the various methods of on-chip mode confinement, heteroepitaxy on SOI (001) substrates seems to be the most promising solution. Not only does it ensure a strong mode confinement inside the as-grown III-V nano-ridges and enable coupling into silicon waveguides, it also facilitates the injection of charged carriers into the active region since the Si device layer could be readily doped. Single-mode lasing could be realized by adopting well-understood mode-selection designs such as distributed Bragg reflectors, distributed feedback cavities, and photonic crystal cavities. With all the basic components ready, electrically driven on-chip telecom nano-lasers will be demonstrated in the near future.

REFERENCES

1. Z. Zhou, B. Yin, and J. Michel, "On-chip light sources for silicon photonics," Light Sci. Appl. **4**, e358 (2015).
2. D. Liang and J. E. Bowers, "Recent progress in lasers on silicon," Nat. Photonics **4**, 511–517 (2010).
3. R. Yan, D. Gargas, and P. Yang, "Nanowire photonics," Nat. Photonics **3**, 569–576 (2009).
4. R. Chen, T. T. D. Tran, K. W. Ng, W. S. Ko, L. C. Chuang, F. G. Sedgwick, and C. Chang-Hasnain, "Nanolasers grown on silicon," Nat. Photonics **5**, 170–175 (2011).
5. D. Saxena, S. Mokkapati, P. Parkinson, N. Jiang, Q. Gao, H. H. Tan, and C. Jagadish, "Optically pumped room-temperature GaAs nanowire lasers," Nat. Photonics **7**, 963–968 (2013).
6. B. Mayer, L. Janker, B. Loitsch, J. Treu, T. Kostenbader, S. Lichtmannecker, T. Reichert, S. Morkotter, M. Kaniber, G. Abstreiter, and C. Gies, "Monolithically integrated high-β nanowire lasers on silicon," Nano Lett. **16**, 152–156 (2015).
7. J. Tatebayashi, S. Kako, J. Ho, Y. Ota, S. Iwamoto, and Y. Arakawa, "Room-temperature lasing in a single nanowire with quantum dots," Nat. Photonics **9**, 501–505 (2015).
8. D. Thomson, A. Zilkie, J. E. Bowers, T. Komljenovic, G. T. Reed, L. Vivien, D. Marris-Morini, E. Cassan, L. Virot, J. M. Fédéli, J. M. Hartmann, J. H. Schmid, D.-X. Xu, F. Boeuf, P. O'Brien, G. Z. Mashanovich, and M. Nedeljkovic, "Roadmap on silicon photonics," J. Opt. **18**, 073003 (2016).
9. B. Tian, Z. Wang, M. Pantouvaki, P. Absil, J. Van Campenhout, C. Merckling, and D. Van Thourhout, "Room temperature O-band DFB laser array directly grown on (001) silicon," Nano Lett. **17**, 559–564 (2016).
10. F. Lu, I. Bhattacharya, H. Sun, T. T. Tran, K. W. Ng, G. N. Malheiros-Silveira, and C. Chang-Hasnain, "Nanopillar quantum well lasers directly grown on silicon and emitting at silicon-transparent wavelengths," Optica **4**, 717–723 (2017).
11. M. Takiguchi, A. Yokoo, K. Nozaki, M. D. Birowosuto, K. Tateno, G. Zhang, E. Kuramochi, A. Shinya, and M. Notomi, "Continuous-wave operation and 10-Gb/s direct modulation of InAsP/InP sub-wavelength nanowire laser on silicon photonic crystal," APL Photon. **2**, 046106 (2017).
12. H. Kim, W. J. Lee, A. C. Farrell, A. Balgarkashi, and D. L. Huffaker, "Telecom-wavelength bottom-up nanobeam lasers on silicon-on-insulator," Nano Lett. **17**, 5244–5250 (2017).
13. Y. Ma, X. Guo, X. Wu, L. Dai, and L. Tong, "Semiconductor nanowire lasers," Adv. Opt. Photon. **5**, 216–273 (2013).
14. A. H. Chin, S. Vaddiraju, A. V. Maslov, C. Z. Ning, M. K. Sunkara, and M. Meyyappan, "Near-infrared semiconductor subwavelength-wire lasers," Appl. Phys. Lett. **88**, 163115 (2006).
15. J. Z. Li, J. Bai, J. S. Park, B. Adekore, K. Fox, M. Carroll, A. Lochtefeld, and Z. Shellenbarger, "Defect reduction of GaAs epitaxy on Si (001) using selective aspect ratio trapping," Appl. Phys. Lett. **91**, 021114 (2007).
16. W. Guo, L. Date, V. Pena, X. Bao, C. Merckling, N. Waldron, N. Collaert, M. Caymax, E. Sanchez, E. Vancoille, and K. Barla, "Selective metal-organic chemical vapor deposition growth of high quality GaAs on Si (001)," Appl. Phys. Lett. **105**, 062101 (2014).
17. C. Merckling, N. Waldron, S. Jiang, W. Guo, N. Collaert, M. Caymax, E. Vancoille, K. Barla, A. Thean, M. Heyns, and W. Vandervorst, "Heteroepitaxy of InP on Si (001) by selective-area metal organic vapor-phase epitaxy in sub-50 nm width trenches: the role of the nucleation layer and the recess engineering," J. Appl. Phys. **115**, 023710 (2014).
18. T. Orzali, A. Vert, B. O'Brian, J. L. Herman, S. Vivekanand, S. S. Papa Rao, and S. R. Oktyabrsky, "Epitaxial growth of GaSb and InAs fins on 300 mm Si (001) by aspect ratio trapping," J. Appl. Phys. **120**, 085308 (2016).
19. Z. Wang, B. Tian, M. Paladugu, M. Pantouvaki, N. Le Thomas, C. Merckling, W. Guo, J. Dekoster, J. Van Campenhout, P. Absil, and D. Van Thourhout, "Polytypic InP nanolaser monolithically integrated on (001) silicon," Nano Lett. **13**, 5063–5069 (2013).
20. B. Kunert, W. Guo, Y. Mols, B. Tian, Z. Wang, Y. Shi, D. Van Thourhout, M. Pantouvaki, J. Van Campenhout, R. Langer, and K. Barla, "III/V nano ridge structures for optical applications on patterned 300 mm silicon substrate," Appl. Phys. Lett. **109**, 091101 (2016).
21. R. Cipro, T. Baron, M. Martin, J. Moeyaert, S. David, V. Gorbenko, F. Bassani, Y. Bogumilowicz, J. P. Barnes, N. Rochat, and V. Loup, "Low defect InGaAs quantum well selectively grown by metal organic chemical vapor deposition on Si (100) 300 mm wafers for next generation non planar devices," Appl. Phys. Lett. **104**, 262103 (2014).
22. Q. Li, Y. Han, X. Lu, and K. M. Lau, "GaAs-InGaAs-GaAs fin-array tunnel diodes on (001) Si substrates with room-temperature peak-to-valley current ratio of 5.4," IEEE Electron Device Lett. **37**, 24–27 (2016).
23. Z. Wang, B. Tian, M. Pantouvaki, W. Guo, P. Absil, J. Van Campenhout, C. Merckling, and D. Van Thourhout, "Room-temperature InP distributed feedback laser array directly grown on silicon," Nat. Photonics **9**, 837–842 (2015).
24. Y. Shi, Z. Wang, J. Van Campenhout, M. Pantouvaki, W. Guo, B. Kunert, and D. Van Thourhout, "Optical pumped InGaAs/GaAs nano-ridge laser epitaxially grown on a standard 300-mm Si wafer," Optica **4**, 1468–1473 (2017).
25. L. Megalini, B. Bonef, B. C. Cabinian, H. Zhao, A. Taylor, J. S. Speck, J. E. Bowers, and J. Klamkin, "1550-nm InGaAsP multi-quantum-well structures selectively grown on v-groove-patterned SOI substrates," Appl. Phys. Lett. **111**, 032105 (2017).
26. S. Li, X. Zhou, M. Li, X. Kong, J. Mi, M. Wang, W. Wang, and J. Pan, "Ridge InGaAs/InP multi-quantum-well selective growth in nanoscale trenches on Si (001) substrate," Appl. Phys. Lett. **108**, 021902 (2016).
27. Y. Han, Q. Li, S. P. Chang, W. D. Hsu, and K. M. Lau, "Growing InGaAs quasi-quantum wires inside semi-rhombic shaped planar InP nanowires on exact (001) silicon," Appl. Phys. Lett. **108**, 242105 (2016).
28. Y. Han, Q. Li, and K. M. Lau, "Highly ordered horizontal indium gallium arsenide/indium phosphide multi-quantum-well in wire structure on (001) silicon substrates," J. Appl. Phys. **120**, 245701 (2016).
29. Y. Han, Q. Li, S. Zhu, K. W. Ng, and K. M. Lau, "Continuous-wave lasing from InP/InGaAs nanoridges at telecommunication wavelengths," Appl. Phys. Lett. **111**, 212101 (2017).
30. M. Paladugu, C. Merckling, R. Loo, O. Richard, H. Bender, J. Dekoster, W. Vandervorst, M. Caymax, and M. Heyns, "Site selective integration of III-V materials on Si for nanoscale logic and photonic devices," Cryst. Growth Des. **12**, 4696–4702 (2012).
31. G. Biasiol, A. Gustafsson, K. Leifer, and E. Kapon, "Mechanisms of self-ordering in nonplanar epitaxy of semiconductor nanostructures," Phys. Rev. B **65**, 205306 (2002).
32. S. Jiang, C. Merckling, W. Guo, N. Waldron, M. Caymax, W. Vandervorst, M. Seefeldt, and M. Heyns, "Evolution of (001) and (111) facets for selective epitaxial growth inside submicron trenches," J. Appl. Phys. **115**, 023517 (2014).
33. Y. Han, Q. Li, K. W. Ng, S. Zhu, and K. M. Lau, "InGaAs/InP quantum wires grown on silicon with adjustable emission wavelength at telecom bands," Nanotechnology **29**, 225601 (2018).
34. D. Cui, S. M. Hubbard, D. Pavlidis, A. Eisenbach, and C. Chelli, "Impact of doping and MOCVD conditions on minority carrier lifetime of zinc-and carbon-doped InGaAs and its applications to zinc-and carbon-doped InP/InGaAs heterostructure bipolar transistors," Semicond. Sci. Technol. **17**, 503–509 (2002).
35. H. Sun, F. Ren, K. W. Ng, T. T. D. Tran, K. Li, and C. J. Chang-Hasnain, "Nanopillar lasers directly grown on silicon with heterostructure surface passivation," ACS Nano **8**, 6833–6839 (2014).
36. N. Waldron, C. Merckling, L. Teugels, P. Ong, S. Ansar, U. Ibrahim, F. Sebaai, A. Pourghaderi, K. Barla, N. Collaert, and A. Voon-Yew Thean, "InGaAs gate-all-around nanowire devices on 300 mm Si substrates," IEEE Electron Device Lett. **35**, 1097–1099 (2014).
37. Y. Han, Q. Li, and K. M. Lau, "Tristate memory cells using double-peaked fin-array III-V tunnel diodes monolithically grown on (001) silicon substrates," IEEE Trans. Electron Devices **64**, 4078–4083 (2017).